Deliverable D3

Title

Validation report for the digital twin software, considering requirements of digitisation and industry 4.0, for static, continuous and dynamic force transfer standards including measurement uncertainty determination

EMPIR Grant Agreement number

18SIB08

Project short name

ComTraForce

Leading partner

Dr. Claudiu Giusca (CU)
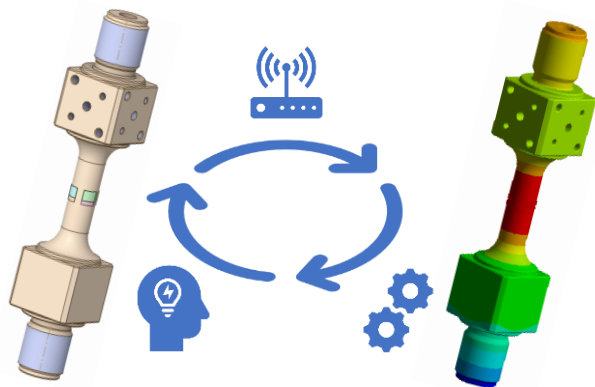
Due date	Submission date
28.02.2022	08.12.2022

DOI: 10.5281/zenodo.7404128

Validation report for the digital twin software, considering requirements of digitisation and industry 4.0, for static, continuous and dynamic force transfer standards including measurement uncertainty determination

Digital Twin Force

Validation report for the digital twin software, considering requirements of digitisation and industry 4.0, for static, continuous and dynamic force transfer standards including measurement uncertainty determination

Version 1.0

Editors

Cranfield University, UK:
  C. Giusca

Physikalisch Technische Bundesanstalt, Germany:
  O. Baer

CEM, Spain:
  C. G. Izquierdo, S. M. González

INRiM, Italy:
  A. Prato

Comprising the results from our research and the fruitful and intensive discussions with all our other project partners worldwide.

Contact: comtraforce@ptb.de

Cranfield February 2023

Table of Contents

1 Executive Summary

The aim of this report is to describe the preliminary version of a digital metrological twin (DMT) of a force measuring device for static, continuous and dynamic forces. In almost all major manufacturing industries such as aerospace, automobile, and construction, one of the most important activities is material/mechanical testing [1], [2]. Material/mechanical testing allows the manufacturer to understand, quantify and check whether their product is suitable for a particular application. This process involves the measurement of force/s acting on a product usually by means of a force measuring instrument called a load cell.

With the inevitability of the fourth industrial revolution, coined as Industry 4.0, virtual tools and models of measuring instruments called digital twins (DT) will be required in manufacturing and inspection processes. A DT is generally defined as "a virtual model used to facilitate detailed analysis and monitoring of physical or psychological systems" [3], see Figure 1. DT's purpose is not to mirror but rather to ensure the "health," integrity and reliability through monitoring, prediction and optimisation of its physical asset using data analytics, artificial intelligence, machine learning, among others.
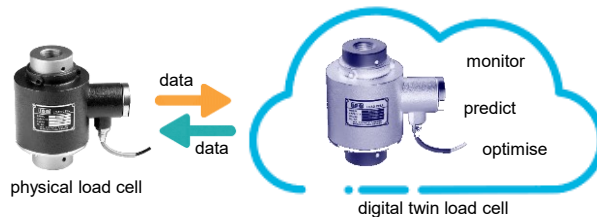
Figure 1 Digital Twin Layout

Sensors placed on the physical asset, for example a load cell, could acquire real-time data through the Internet of Things (IoT)

network. The data are then used either in simulations or dashboards of information which will act as the load cell's DT. The DT is capable of providing next-level prediction, monitoring, and recommendation to conduct real time root cause analysis to avert failures of the load cell [4], [5], [6] and [7].

Creep is a recognised phenomenon in load cells that has a tendency to limit the reliability and accuracy of the instrument. It is the "*change in output occurring with time while under constant load and with all environmental conditions and other variables also remaining constant*" [14].

Different geometrical models of the force transducer were used for different DT models. Simplified models of the cylindrical shape load cell were used to perform analytical stress-strain analysis of the transducer under stating loading and to determine creep strain rate of transducer materials. Another reason for transducer geometry variation is the transducer adjustment. For the static calibration test the transducer with the ringlike masses mounted on the shaft shoulders was used. During the project, the calibration setup was improved in the way the shaft shoulders were replaced with holes directly drilled in the selected spot of the transducer. The measurement with the improved transducer could be taken also without masses or alternatively with cube masses [33]. The improved set up without masses was used for continuous as well as dynamic models, see sections 4 and 5 respectively.

Section 2 summarises the way in which creep strain can be used to monitor and optimise load cell behaviour in the DT context. Findings presented in this section indicate that the major source of creep in load cells is the carrier matrix of the strain gauge, although very small - a few ppm per hour, and that the Larson-Miller Parameter equation can be used to support the development of the DT for the load cell.

Section 3 describes the development of a DT concept with a focus on a metrological application case. To enable the application of DT concept in metrological field the input parameters were read from Digital Calibration Certificate (DCC) of a force measurement device. This enabled that parameters were related to a SI unit as well as measurement uncertainty. The DT FEA models were validated with the traceable calibration measurements, performed at PTB. The issue of data storage was addressed in the concept but not realised at this stage.

Additionally, the communication strategies based on Python that can be employed in a DMT of a load cell are discussed, along with potential use of artificial intelligence (AI) tools that could be used in the future to improve the force sensor output and its associate measurement uncertainties.

Section 4 reports on the development and validation of a FEM model describing the static calibration model of the load cell. The FEA static model was found to be in good agreement with the analytical formulation, however large discrepancies exist between ether models and experimental results, which include additional error sources, such as: amplifier and data acquisition errors, temperature, sensitivity stability, interpolation resolution [8]. Nevertheless, FEM model is in particular useful to investigate the effect of the shape of the load cell on the strain measurements as well as the effect loading conditions, identified as bending moments, tilt and side forces. Even though the static calibration measurement procedure is designed to evaluate the transducers with minimum creep effect, the creep will inadvertently affect the measurement accuracy.

Section 5 addresses the thermal creep associated with the loading and unloading operations. As previously recorded in literature, the thermo-mechanical effect is responsible with heating and cooling the load cell during loading and unloading operation, respectively. The findings are in agreement with the

current knowledge related to the creep behaviour experienced in force transducers. The creep evaluated in [8] is governed by the strain gauge relaxation behaviour, which in this case was not adequately matched with the thermal creep of the load cell (see the creep graphs presented in section 5).

Section 6 presents the FEM model that is used to evaluate the sensor behaviour under cyclic loading. The FEM simulations were able to reproduce the range of temperature variations previously reproduced experimentally, which once again are attributed thermomechanical effects. Here, the effectiveness of the simulations was hindered by the computational limitations required by FEM.

Section 7 concludes the report, summarising briefly the main findings of the research and mapping the way in which the FEA models can be used in the development of numerical oriented force uncertainty models.

2 Creep of load cell materials

Creep occurs in all materials in stages; however, they differ on how fast it occurs. The three typical stages of creep are shown in Figure 2 [9]:
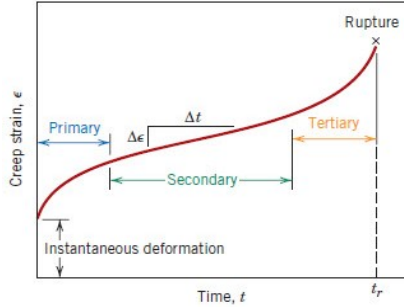

Figure 2 A typical creep curve with three stages

It is acknowledged that creep is mainly evaluated through its creep rate in the secondary stage due to its dominance and long-term occurrence in the creep curve compared to the other stages [10]. Engineers use this information as a point of performance comparison between materials and design for safety assurance by predicting creep behaviour for a particular application. Engineers make use of steady state creep rate $\dot{\varepsilon}_{cr}$ for prediction and extrapolation at different temperatures, and commonly used form of the equation is:

$$\dot{\varepsilon}_{cr} = K\sigma^n e^{\left(\frac{-Q_c}{RT}\right)} \tag{2.1}$$

known as the power law equation where K is a constant, σ is the applied stress, n gives the stress dependence of the strain rate, Q_c is the creep activation energy, R is the universal gas constant, and T is the absolute temperature [11]. However, the constants K and n are determined using the existing steady state creep rate obtained from creep data at different stresses and

temperatures. This equation is generally used for dislocation and diffusion creep, frequently occurring in metals [12].

Another popular approach is using the Larson-Miller Parameter to determine the steady state creep rate. Similar to the power law, it uses existing steady state creep rates obtained from creep data at different stresses and temperatures. The LMP is given as:

$$\text{LMP} = T\left(C - log(\dot{\varepsilon}_{\text{cr}})\right) \tag{2.2}$$

where T is the temperature, $\dot{\varepsilon}_{\text{cr}}$ is the steady state creep rate and C as the empirical constant which can be obtained from two creep tests conducted at different temperatures but same stress. J. Li and A. Dasgupta's work provided the value of C as - 3.0 [12]. A master curve is then plotted to show the relationship between the applied stress and LMP. The curve is then used to extrapolate the value of LMP at any given stress to determine the steady state creep rate at any temperature:

$$\dot{\varepsilon}_{\text{cr}} = 10^{C - \frac{\text{LMP}}{T}} \tag{2.3}$$

The dependence of creep in polymers on temperature and time makes the LMP suitable for use with polymers [12].

2.1 Geometrical set up of load cell and material properties

This research chose the strain gauge load cell as it is widely used for its accuracy and lower unit cost compared with other types of load cells [13], and it has been the primary focus of the development of the OIML Recommendation 60 [14]. To investigate the dominant source of creep in strain gauge load cells, the load cell was isolated into two major components: the cylindrical shape spring element and the strain gauge. The strain

gauge will be represented by its carrier matrix since the measuring grid does not contribute to the creep on the strain gauge, and the carrier matrix makes up most of the strain gauge [2], [16]. For simplicity, the adhesive of the strain gauge was assumed to be part of the carrier matrix and made of the same material [15], see Figure 3.
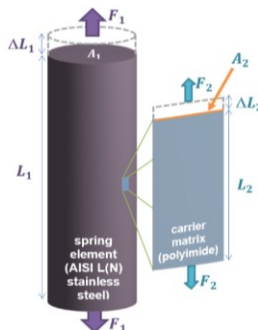
Figure 3 Strain gauge load cell by Hunt et al showing applied loads and resulting elongations

The basic specifications of the hypothetical 0.5 MN strain gauge load cell used in this research are found in Table 1.

Table 1 Specifications of the hypothetical 0.5 MN Load Cell

Parameter	Spring Element	Carrier Matrix
Shape	cylinder	rectangular
Material	AISI 316 L(N) stainless steel	polyimide
Young's Modulus	190 GPa	2.5 GPa
Yield Point	-	69 MPa
Height	140 mm	7.5 mm
Diameter	43 mm	-
Width	-	4.6 mm

Thickness	-	30 µm

2.1.1 Determination of Creep Rate in the load cell components at Room Temperature

The power law given by equation (2.1) has been used to estimate the creep rate in the *spring element* of the load cell at room temperature. For this purpose, the experimental data from the work of Reith *et al.* [17] on the creep behaviour of AISI 316 L(N) stainless steel was used, which allowed the estimation of the creep rate.

The least-square fit method was used in determining the constants of the power law since it assures a more accurate estimation of the constants as it uses all the data points rather than just selected sets [18]. The constants obtained are found in Table 2.

Table 2 Summary of constants for the spring element using the least square fit method

K	7.38×10^3 h^{-1}
n	6.96
Q_c	460 kJ/mol

The extrapolation method by LMP was used to determine the creep rate in the *carrier matrix* given by equation (2.2). J. Li and A. Dasgupta used the experimental creep data of X. Wu and M. Pecht [19] to obtain the empirical constant *C* and creep rates of polyimide. They then used these data to develop an LMP Master Curve for polyimide. Here, the master curve was reconstructed to extract the equation of the resulting trend line, Figure 4.
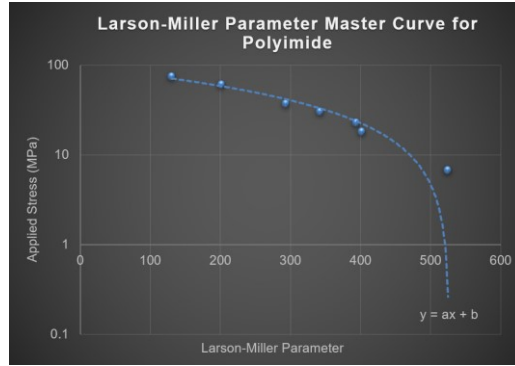
Figure 4 LMP master curve for polyimide

From the equation of the line, the LMP can be determined at a given stress by:

$$x = \frac{y - b}{a} \qquad\qquad (2.4)$$

where x = LMP, y is the applied stress, a = -0.1792, and b = 94.266.

2.1.2   Equivalent Stress Acting on the Carrier Matrix

There is a need to determine the equivalent stress acting on the carrier as a force or stress is exerted at the spring element. Figure 3 is the diagram of the load cell with its spring element and carrier matrix and the relationships between different parameters, where F_1 is the force acting on the hypothetical 0.5 MN load cell, L_1 is the length of the spring element, ΔL_1 is the change in length of the spring element due to F_1, A_1 is the area of the spring element where the F_1 is acting on, F_2 is the force acting on the carrier matrix, L_2 is the length of the carrier matrix, ΔL_2 is the change in length of the carrier matrix due to F_2 and A_2 is the area of the carrier matrix where F_2 is acting on.

Using the Young's Modulus equation:

$$E = \frac{FL_o}{A\Delta L} \tag{2.5}$$

where F is the force applied, L_o is the original length, A is the area where the force is applied, and E is the Young's Modulus of the material, the value of ΔL_1 can be determined by rearranging equation (2.5) into:

$$\Delta L_1 = \frac{F_1 L_1}{A_1 E_{sp}} \tag{2.6}$$

where E_{sp} is the Young's Modulus of AISI L(N) stainless steel. Having ΔL_1, equation (2.7) is used to determine ΔL_2 of the load cell.

$$\Delta L_2 = \frac{\Delta L_1 L_2}{L_1} \tag{2.7}$$

The force acting on the carrier matrix (F_2) can now be determined by rearranging the Young's Modulus equation (2.5) into:

$$F_2 = \frac{E_{cm} A_2 \Delta L_2}{L_2} \tag{2.8}$$

where E_{cm} is the Young's Modulus of polyimide. With this, the stress acting on the carrier matrix can now be computed by dividing the force on the carrier matrix (F_2) by the area of the carrier matrix (A_2). Keying in the stress values to equation (2.4) provides the corresponding LMP (Table 3).

Table 3 Corresponding LMP values for the force on the hypothetical 0.5 MN load cell

Force on the Load Cell, (MN)	Equivalent Stress on the Load Cell, (MPa)	Equivalent Stress on Carrier Matrix, (MPa)	LMP
0.50	344.30	4.53	501
0.40	275.44	3.62	506
0.30	206.58	2.72	511
0.20	137.72	1.81	516
0.10	68.86	0.91	521

2.2 Results

The equivalent stress on the spring element is needed to extrapolate the creep rate using equation (2.1). This was determined by dividing the force applied by the area where the force is applied. Finally, extrapolating at the usual working temperature of a load cell (generally 293 K) using equation (2.1) with the constants in Table 2 yields the creep rates of the spring element at different forces and equivalent stresses. The experimental creep rates from Reith *et al.* [17] and computed creep rates in the spring element were compared to validate the constants used. It was seen that the differences in values were at 54 % for 923 K, 46 % for 973 K, and 230 % for 1,023 K. These significant differences appear at the higher stress values, whereas in the middle range, the stress values are well predicted. These differences might be due to the lack of data or coverage of the trend to acquire a better estimation of the constants, which is typical during extrapolation or from the errors via the experimental set-up or other factors affecting the outcome of the experimental results.

In the same manner, having the LMP makes it possible to extrapolate the creep rates of the carrier matrix at the usual working temperature of a load cell (generally 293 K) using equation (2.3). The computed creep rates of the spring element and the carrier matrix, presented in Table 3, show that the dominant source of creep originates from the carrier matrix.

Table 4: Calculated creep rates in the spring element and carrier matrix at a given force on the strain gauge load cell

Force on Load Cell (MN)	Creep Rate in the Spring Element (h^{-1})	Creep Rate in the Carrier Matrix (h^{-1})
0.50	≈ 0 (3×10^{-58})	1.95×10^{-05}
0.40	≈ 0 (7×10^{-59})	1.88×10^{-05}
0.30	≈ 0 (9×10^{-60})	1.80×10^{-05}
0.20	≈ 0 (5×10^{-61})	1.73×10^{-05}
0.10	≈ 0 (4×10^{-63})	1.67×10^{-05}

2.3 Determination of the operating parameters of load cells for use in the DT

With the carrier matrix identified as the dominant source of creep in strain gauge load cells at room temperature, the stress-strain curve of polyimide [20] was used to identify the strain due to creep before the strain gauge enters a state where it cannot go back to its original length/shape called plastic deformation.
The strain was determined using equation (2.9):

$$\varepsilon = \frac{\sigma}{E} \qquad (2.9)$$

where ε is the strain at yield point (69 MPa for polyimide), and E is the Young's Modulus (2.5 GPa for polyimide). Therefore, the strain at which the carrier matrix undergoes plastic deformation is 2.76 % or 0.0276, Figure 5. Although the strain of the spring element is likely to be smaller, it should be noted that the deformation, in this case, should be governed by stress and not strain. The spring element will still be in the elastic regime at 69 MPa of stress and will not be much affected; however, that amount of stress is sufficient for enforcing the polyimide by a strain of magnitude 2.76 %. As the spring element is still within the elastic limit, the carrier matrix under a stress of 69 MPa may already be experiencing plastic deformation.
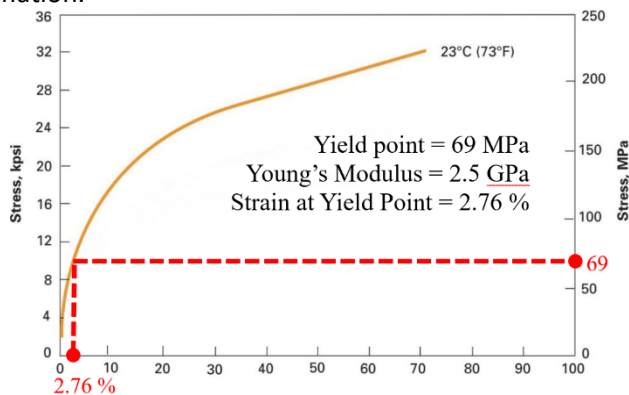

Figure 5 Dupont's stress-strain curve of polyimide

2.3.1 Numerical Model of the DT Load Cell for Creep Strain

The LMP equation (2.3) served as the numerical model after confirming that the strain gauge's carrier matrix is the primary source of creep. Equation (2.10) shows the expanded version of equation (2.3) by using equation (2.4) to replace LMP:

$$\dot{\varepsilon}_{cr} = 10^{C-\left(\left(\frac{\frac{F}{A}-b}{a}\right)/T\right)} \tag{2.10}$$

where F is the force applied on the carrier matrix, A is the area where the force is applied, a = -0.1792, b = 94.266, T is the temperature, and C = -3.0 (empirical material constant for polyimide).

The area where force is applied A and the empirical constant C has been predetermined and inputted in the numerical model, so it only requires two essential inputs to build the DT load cell for creep strain: the force applied on the carrier matrix F and temperature T, Figure 6.
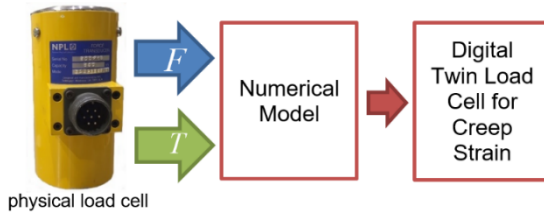
Figure 6 Development of the Digital Twin Load Cell for Creep Strain

The force applied to the carrier matrix can be computed using the method shown in the Equivalent Stress Acting on the Carrier Matrix section, as it receives force measurement data in real-time from the physical load cell. The temperature can be determined by attaching a temperature sensor to the load cell (real-time). This assumes that the spring element's temperature equilibrates with the carrier matrix. With all inputs available, it is possible to determine the creep rates to provide the creep strains. Creep strains were determined by multiplying the creep rate by how long the force is applied. The creep strains were plotted against the force applied to the load cell and the amount of time the force was applied.

2.3.2   Supporting the Development of the DT for Load Cell

A DT need not be a virtual image of the physical measuring instrument. Instead, the resulting DT in this research is represented by a three-dimensional graph in terms of creep strain at the carrier matrix, force applied on the load cell, and amount of time the force is applied.

Figure 7 was developed using Originlab 2019b. The graph represents the DT load cell for the monitoring of creep strain and illustrates the operating range of a 0.5 MN capacity load cell with the indication that the creep strain must not exceed 0.0276 when used at room temperature (293 K).
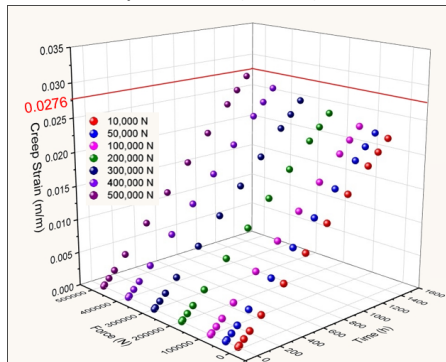

Figure 7 Digital Twin Load Cell for Creep Strain

Through trial and error, it was revealed that at a maximum load of 0.5 MN, the strain gauge would undergo plastic deformation if the force is applied to the load cell for more than 1,400 hours since the strain at this time is already 2.76×10^{-02}. If the strain gauge reaches this state, the whole load cell has a high risk of becoming defective. Although the usual duration of use of most load cells is not more than two hours, there are applications where load cells are under constant loads for days, such as a calibration system for Coriolis flow meters by

volumetric and gravimetric methods and inventory monitoring of storage silos [2], [21].

The graph also indicates that time influences the creep strain more than the force applied to the load cell. Even at maximum capacity, the creep strain is still lower after one hour compared to an applied force of only 0.01 MN after ten hours. This may look contradictory, but it should be noted that the creep strain at the strain gauge (carrier matrix) is determined by the equivalent stress, which is only 1.31 % of the stress acting on the load cell (Table 3).

3 Digital Twin Concept

In the following section the frameworks for the development of the DT of force measurement device are discussed. As the starting point the requirements of digitization and Industry 4.0 describe secure and unambiguous exchange of the metrological data. Based on these, the requirements for DT for metrological application are formed. The way of data communication and synchronization in metrological digital world is proposed. A key role in the data communication of a DMT plays a force DCC.

3.1 Requirements of digitization and Industry 4.0

DT software must fulfil the requirements of digitization and Industry 4.0 in order to ensure the quality of exchanged data as well as its security. In the completed EMPIR project SmartCom "Communication and validation of metrological smart data in IoT-networks" [22] the main requirements were formulated as follows:

1. Requirements on measurement data quality [23]:
   - Use of Universal Data Format.
   - For the digital exchange of metrological data, it is essential to associate at least one value to a corresponding Unit [SI Unit].
   - The complete indication of a measured quantity may contain additional information such as a specification of measurement uncertainty and a time stamp.
2. Secure data exchange requirements [24].
   - authenticity;
   - completeness of the transmitted data;
   - data integrity;

- manipulation protection as well as protection of confidentiality.

Taking into consideration above mentioned requirements for data communication, the requirements on a DMT were formulated as following [25]:

1. The measurement uncertainty is calculated according to recognized standards;
2. All input parameters are traceably determined and stated with the corresponding measurement uncertainty;
3. And it is validated by traceable measurements.

3.2   Digital Metrological Twin

Digital Metrological Twin (DMT) build based on the requirements stated in subsection above will provide the output which can be utilised in metrological services. DMT is the enhanced way to generate, process and store data on calibration device with the time stamp. Beyond the concept of a DCC [26], where calibration data is collected, DMT allows to correlate the force transducer output with the physical processes occurring in the transducer and allows its seamless connection with the factory of the future. All relevant data in such database is traceable and represented with SI units, if applicable. This data can be used by the end user in the further life-cycle of the calibrated device. Furthermore, the use of DMT will allow calibration system to learn from itself and improve the measurements uncertainty for future calibration processes with the same device as well as deliver data to derive correlations between calibration conditions, mounting, etc. as well as output values for devices of the similar class.

The force measurement device DMT is based on the concept of Grieves [27] and Vickers [28] and covers three main functions, see Figure 8. The first function allows for a prompt reading of

selected device information, e. g. sensors reading (temperature, strain sensors). Here the key role plays the speed of communication as well as preservation of data quality. The physical-to-virtual communication is realised by reading of relevant device information from a DCC for force measurement. The second function of DT is the data processing by means of one of three models, mentioned above. The main outcome of data processing is the prediction of force measurements device output as well as measurement uncertainty.
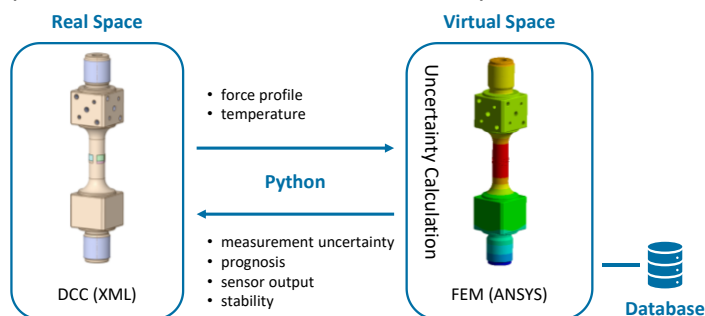
Figure 8 Concept of DMT of force measurement device

For the DMT it is crucial that the input / output parameters are traceable and are stated with the corresponding measurement uncertainty. Additionally, the validation of the static, continuous and dynamic models within DT must be performed using traceable measurements. The third function enables saving of the modelled output which can be used to recalculated uncertainty in future calibration procedures.

As the first prototype of the DMT of force measurement device, the FEM model of the transducer is developed. The models of static, continuous and dynamic calibration processes are developed in FE simulation software, see sections 4, 5 and 6 respectively. The synchronization between the force measurement device and its DT is performed after each

calibration process in form of reading and subsequent update of the DCC by means of Python programming. The calculated with DT device output as well as measurement uncertainty are saved after each calibration in a database. The corresponding database of DT represents the device history, allowing the DT to recall any state of the device history.

3.3　Data Communication

Data Input

The physical-to-virtual communication is realised by reading of relevant device information from a DCC in XML format. The benefit of direct use of data from DCC is that the results data is provided in SI format. The data transfer from DCC ensures that the input parameters of DT are traceable and stated with the given measurement uncertainty, as required by the definition of DMT. The DCC for static force calibration was developed by PTB according to the XML scheme (XSD) 3.1.2 [29]

To read input parameters from DCC in XML format the ElementTree XML API of Python was used. It allows to read the specified elements of DCC XML tree, see Figure 9.

Figure 9 XML structure of force DCC and highlighted list element containing values of applied force magnitude

ET.parse command was used to navigate to DCC document. The *.getroot()* command gets the parent tag of the XML document. The children nodes can be specified by the index, as it is shown in the example below:

root[1][0][3][3][1][0][0][1][0].text

Identifier *.text* allows to access the text of the specified child element. The force magnitude from DCC is then written to .txt file for further transfer to ANSYS FE-model as a boundary condition. Further input parameters such as temperature, frequency, mass, etc. can be extracted in a similar manner. Python code is used to automatically built the entire FE-model, select data for output and run the simulation [30].

Data output and storage

The calculated with the DT force transducer data is used to calculate measurement uncertainty considering effects from mechanical system, surrounding the force measurement device. In future developments, the collection of the selected information to a database will be realised. Each dataset will be completed with the metadata stating the calibration time. In this way the continuous calibration history of the force measurement device will be created.

3.4   Machine Learning Models

Machine learning models provide solutions to problems with high number of depending parameters. However, depending on the architecture of the Neural Network implemented (as Deep Neural Networks) a huge number of training data is required. As the number of training data increase the training time increase, but results provide from the model improves.

Another parameter to optimize is the number of epochs (number of times that the neural network is going to do the training). It is necessary to stablish which is a high and low number of epochs for each model, as a high number of epochs for a model can result in over training (the model is only trained for the training data and it cannot predict another values). Also not enough training ends in a similar situation. It is necessary to highlight a linear increase in training time with the number of epochs, as it is shown in the Figure 10.
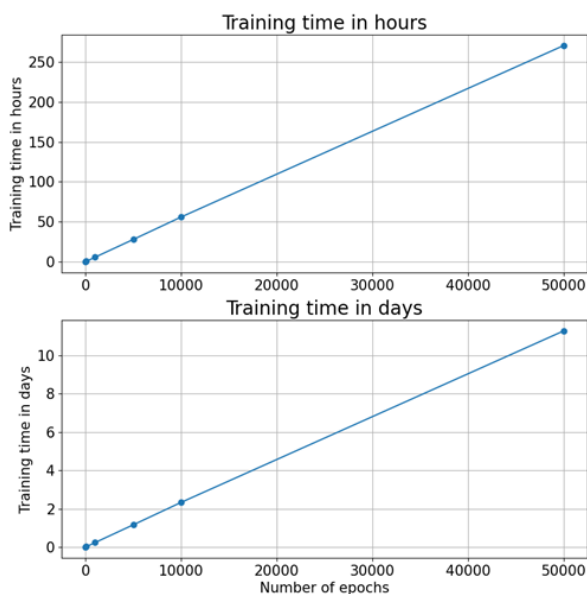

Figure 10: Evolution of training time with the number of epochs for a LSTM-layer-based model with 100 input data trained with a workstation with a CPU Intel Xeon 6230R, GPU NVIDIA Quadro RTX 8000 and 128 Gb of RAM.

If a high number of training examples is not possible new architectures of Neural Networks and new training techniques can be implemented to solve this problem.

4 Static calibration test model

In the following section the FEA model of static calibration test of a 20 kN load cell is presented. The model was developed with the focus on further application in DT construct. At the first approach an analytical solution for the simplified case of a cylindrical shape transducer was derived. The analytical solution was then compared with the FEM analysis, performed with the ANSYS software. In the second step, the real geometry transducer model was numerically studies in ABAQUS software. To validate the model the results obtained from ABAQUS [31] FEA static implicit solver and an analytical solution were compared with the calibration data of the sensor in accordance with the ISO 376:2011-09 [32].

4.1 Analytical stress-strain analysis of the cylindrical force transducer

The unconfined tension of the 20 kN column-type force transducer (CFT) is also studied from the analytical point of view, assuming the principle of superposition and using the relationships underlying linear elasticity and small deformations. The transducer is composed of a cylindrical elastic element, where d and h represent the diameter and the height, respectively of 12 mm and 30 mm, with 4 strain gauges located around the transducer at a height of $h/6$ for the evaluation of the vertical force, as shown in Figure 11.
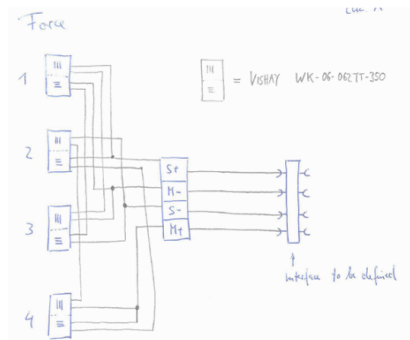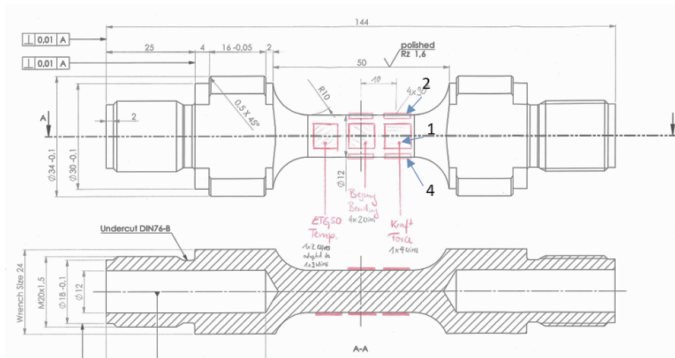
Figure 11 Strain gauge location and bridge wiring of the CFT

Considering a set of forces and bending moments (vertical and side forces/moments) applied to the upper face of the transducer. According to the chosen reference system in Figure 12, F_z in compression is negative, while F_z in tension is positive.
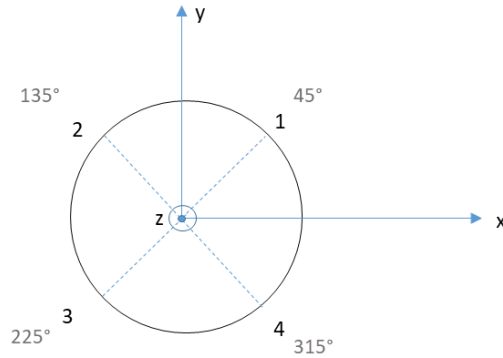
Figure 12 Reference system and strain gauges locations

Strain gauges, sensitive to vertical stress σ_z, are strain gauges 1, 2, 3 and 4 (nominally equal), located at an angle of 45°, 135°, 225° and 315°, with respect to the *x*-axis.

In general terms, the vertical stress σ_{z_i} along z-axis, caused by the vertical force in tension and by possible spurious components (side forces and moments), at i^{th} strain gauge position on the transducers, is given by:

$$
\begin{aligned}
\sigma_{z_i} &= \frac{4F_z}{\pi d^2} - \frac{d}{2I}\left[\cos\theta\left(M_y + F_x\frac{h}{2}\right)\right.\\
&\left.+ \sin\theta\left(-M_x + F_y\frac{h}{2}\right)\right] = \\
&= \frac{4F_z}{\pi d^2} - \frac{d}{2}\frac{1}{\frac{\pi}{4}\left(\frac{d}{2}\right)^4}\left[\cos\theta\left(M_y + F_x\frac{h}{2}\right)\right.\\
&\left.+ \sin\theta\left(-M_x + F_y\frac{h}{2}\right)\right] = \\
&= \frac{4F_z}{\pi d^2} - \frac{32}{\pi d^3}\left[\cos\theta\left(M_y + F_x\frac{h}{2}\right)\right.\\
&\left.+ \sin\theta\left(-M_x + F_y\frac{h}{2}\right)\right]
\end{aligned}
$$

(4.1)

where I is the area moment of inertia of a cylinder and θ is the position angle of each strain gauge.

For strain gauges 1, 2, 3 and 4, the vertical stress σ_{z_i} in tension is therefore given by:

$$\sigma_{z_1} = \frac{4F_z}{\pi d^2} - \frac{32}{\pi d^3} \left[\frac{\sqrt{2}}{2} \left(M_y + F_x \frac{h}{6} \right) \right.$$
$$\left. + \frac{\sqrt{2}}{2} \left(-M_x + F_y \frac{h}{6} \right) \right] \qquad (4.2)$$

$$\sigma_{z_2} = \frac{4F_z}{\pi d^2} - \frac{32}{\pi d^3} \left[\frac{\sqrt{2}}{2} \left(-M_y - F_x \frac{h}{6} \right) \right.$$
$$\left. + \frac{\sqrt{2}}{2} \left(-M_x + F_y \frac{h}{6} \right) \right] \qquad (4.3)$$

$$\sigma_{z_3} = \frac{4F_z}{\pi d^2} - \frac{32}{\pi d^3} \left[\frac{\sqrt{2}}{2} \left(-M_y - F_x \frac{h}{6} \right) \right.$$
$$\left. + \frac{\sqrt{2}}{2} \left(M_x - F_y \frac{h}{6} \right) \right] \qquad (4.4)$$

$$\sigma_{z_4} = \frac{4F_z}{\pi d^2} - \frac{32}{\pi d^3} \left[\frac{\sqrt{2}}{2} \left(M_y + F_x \frac{h}{6} \right) \right.$$
$$\left. + \frac{\sqrt{2}}{2} \left(M_x - F_y \frac{h}{6} \right) \right] \qquad (4.5)$$

In general terms, the strain can be obtained according to:

$$\varepsilon_{z_i} = \frac{\sigma_{z_i}}{E} + \frac{F_x \left(\frac{h}{6} \right)^2 \frac{d}{2}}{2EI} \frac{\frac{d}{2}}{\frac{h}{6}} \cos \theta + \frac{F_y \left(\frac{h}{6} \right)^2 \frac{d}{2}}{2EI} \frac{\frac{d}{2}}{\frac{h}{6}} \sin \theta = \qquad (4.6)$$

$$= \frac{\sigma_{z_i}}{E} + \frac{F_x \left(\frac{h}{6}\right)^2}{2E\frac{\pi}{4}\left(\frac{d}{2}\right)^4} \frac{3d}{h} \cos\theta + \frac{F_y \left(\frac{h}{6}\right)^2}{2E\frac{\pi}{4}\left(\frac{d}{2}\right)^4} \frac{3d}{h} \sin\theta$$

$$=$$

$$= \frac{\sigma_{z_i}}{E} + \frac{8F_x h}{3E\pi d^3} \cos\theta + \frac{8F_y h}{3E\pi d^3} \sin\theta$$

where E is the Young's modulus of the steel elastic element (210 GPa). At each strain gauge position, strain is therefore given by:

$$\varepsilon_{z_1} = \frac{4F_z}{E\pi d^2} - \frac{32}{E\pi d^3}\left[\frac{\sqrt{2}}{2}\left(M_y + F_x \frac{h}{6}\right)\right.$$
$$\left. + \frac{\sqrt{2}}{2}\left(-M_x + F_y \frac{h}{6}\right)\right] \qquad (4.7)$$
$$+ \frac{8F_x h}{3E\pi d^3}\frac{\sqrt{2}}{2} + \frac{8F_y h}{3E\pi d^3}\frac{\sqrt{2}}{2}$$

$$\varepsilon_{z_2} = \frac{4F_z}{E\pi d^2} - \frac{32}{E\pi d^3}\left[\frac{\sqrt{2}}{2}\left(-M_y - F_x \frac{h}{6}\right)\right. \qquad (4.8)$$
$$\left. + \frac{\sqrt{2}}{2}\left(-M_x + F_y \frac{h}{6}\right)\right]$$
$$- \frac{8F_x h}{3E\pi d^3}\frac{\sqrt{2}}{2} + \frac{8F_y h}{3E\pi d^3}\frac{\sqrt{2}}{2}$$

$$\varepsilon_{z_3} = \frac{4F_z}{E\pi d^2} - \frac{32}{E\pi d^3}\left[\frac{\sqrt{2}}{2}\left(-M_y - F_x \frac{h}{6}\right)\right.$$
$$\left. + \frac{\sqrt{2}}{2}\left(M_x - F_y \frac{h}{6}\right)\right] \qquad (4.9)$$
$$- \frac{8F_x h}{3E\pi d^3}\frac{\sqrt{2}}{2} - \frac{8F_y h}{3E\pi d^3}\frac{\sqrt{2}}{2}$$

$$\varepsilon_{z_4} = \frac{4F_z}{E\pi d^2} - \frac{32}{E\pi d^3}\left[\frac{\sqrt{2}}{2}\left(M_y + F_x\frac{h}{6}\right)\right.$$
$$\left. + \frac{\sqrt{2}}{2}\left(M_x - F_y\frac{h}{6}\right)\right] \quad\quad (4.10)$$
$$+ \frac{8F_x h}{3E\pi d^3}\frac{\sqrt{2}}{2} - \frac{8F_y h}{3E\pi d^3}\frac{\sqrt{2}}{2}$$

In this way, it is possible to relate the (mV/V) bridge output with the geometrical parameters of the elastic element (E=210 GPa and v=0.3) and the generated force by knowing the bridge wiring and the gauge factor (k=2) of the strain gauges, according to:

$$\left(\frac{\Delta V}{V}\right) = \frac{k(1+v)}{4}\left(\varepsilon_{z_1} + \varepsilon_{z_2} + \varepsilon_{z_3} + \varepsilon_{z_4}\right)$$
$$= k(1+v)\frac{4F_z}{E\pi d^2} \quad\quad (4.11)$$

By way of example, considering (4.11) different boundary conditions (or tests) in terms of generated vertical forces and spurious side forces and bending moments and applying the above-mentioned equations, it is possible to get the stress-strain values at each strain gauge position and the bridge output, as shown in Table 5. The same mechanical conditions are applied to a simulation software (ANSYS-Fluent), which considers the transducer as a simple cylinder, in order to compare strains and bridge output results at each strain gauge location. As an example, the simulated deformations (to be divided by the length to get the strain) at strain gauge locations of test 3 (F_x=2000 N, F_y=-1000 N, F_z=10000 N, M_x=0 Nm, M_y=0 Nm), are shown in Figure 13.
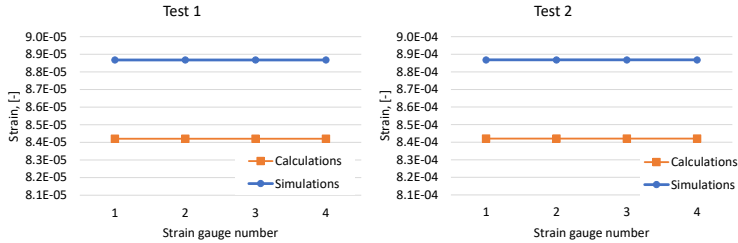
Table 5 Comparison between calculated and simulated strains at strain gauge locations *for the different tests*

Test	Force/moment components					Stress calculation				Strain calculation					Bridge output + Calculation	Strain simulation					Bridge output Simulations
	Fx / N	Fy / N	Fz / N	Mx / N m	My / N m	σ₁ / Pa	σ₂ / Pa	σ₃ / Pa	σ₄ / Pa	e₁ / -	e₂ / -	e₃ / -	e₄ / -	etot / -	ΔV/V / mV/V	e₁ / -	e₂ / -	e₃ / -	e₄ / -	etot / -	ΔV/V / mV/V
1	0	0	2000	0	0	1.77 E+07	1.77 E+07	1.77 E+07	1.77 E+07	8.42 E-05	8.42 E-05	8.42 E-05	8.42 E-05	3.37 E-04	0.22	8.66 E-05	8.66 E-05	8.66 E-05	8.66 E-05	3.46 E-04	0.23
2	0	0	20000	0	0	1.77 E+08	1.77 E+08	1.77 E+08	1.77 E+08	8.42 E-04	8.42 E-04	8.42 E-04	8.42 E-04	3.37 E-03	2.19	8.66 E-04	8.66 E-04	8.66 E-04	8.66 E-04	3.46 E-03	2.25
3	2000	-1000	10000	0	0	2.59 E+07	2.76 E+08	1.51 E+08	9.91 E+07	2.72 E-04	8.68 E-04	5.70 E-04	2.55 E-05	1.68 E-03	1.09	2.95 E-04	9.32 E-04	5.71 E-04	7.35 E-05	1.72 E-03	1.12
4	0	0	10000	-500	400	- 3.66 E+09	- 3.28 E+08	3.84 E+09	5.05 E+08	- 1.74 E-02	1.56 E-03	1.83 E-02	2.41 E-03	1.68 E-03	1.09	- 1.78 E-02	2.46 E-02	1.87 E-02	1.61 E-03	2.00 E-05	1.05
5	2000	-1000	10000	-500	400	- 3.73 E+09	1.41 E+08	3.90 E+09	3.18 E+08	- 1.76 E-02	1.12 E-02	1.84 E-03	1.96 E-03	1.68 E-03	1.09	- 1.78 E-02	2.46 E-02	1.87 E-03	1.61 E-03	2.00 E-05	0.59
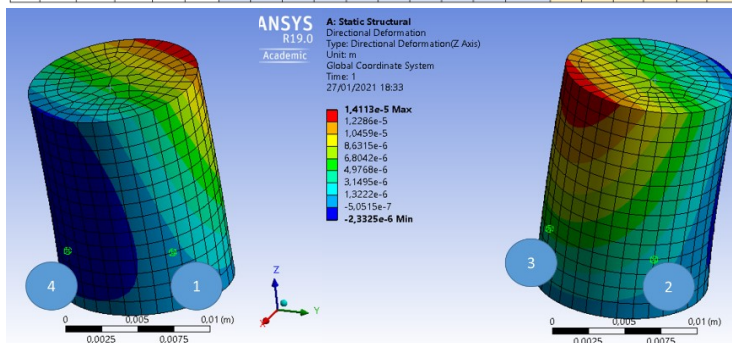
Figure 13 Simulated deformations (in m) at four strain gauge locations for test 3

Comparison between calculation and simulations, depicted in Figure 14-Figure 16, at each strain gauge position, shows a good agreement, with relative differences in the order of 5 %.

Figure 14 Comparison between analytically calculated and simulated strains for tests 1 and 2
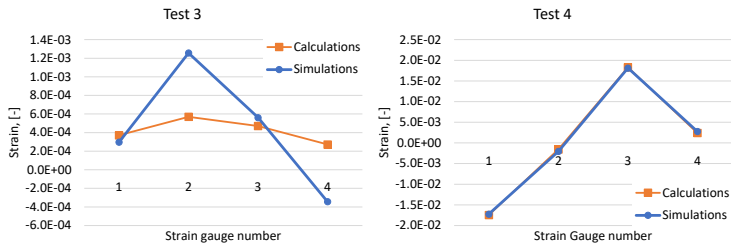
Figure 15 Comparison between calculated and simulated strains for tests 3 and 4
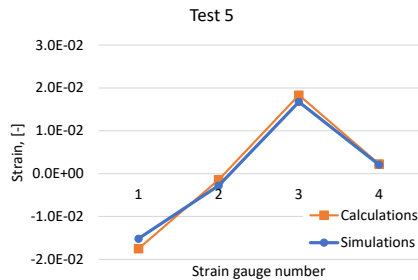
Figure 16 Comparison between calculated and simulated strains for test 5

4.2   Real force transducer model set up

The detailed design of the load cell geometry is described elsewhere [33]. Figure 17 presents a schematic drawing of the load cell with ringlike masses, relative position of the strain gauges (force and bending) and temperature sensor, as well as typical boundary condition used in ABAQUS.
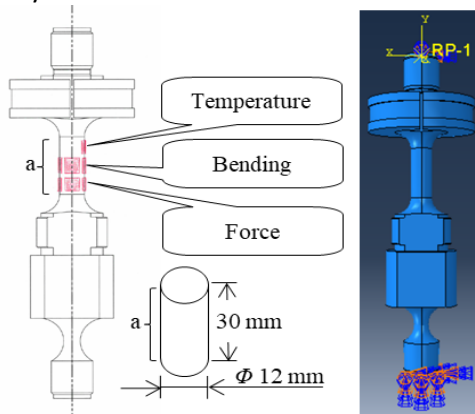

Figure 17 Left - Load Cell schematic and the nominal position of the strain gauges [31]. Right – ABAQUS boundary conditions example

Four strain gauges measuring the longitudinal (L) and transversal (T) strains were connected in a Wheatstone bridge configuration as shown in Figure 18. The four strain gauges were mounted at 90 ° to each other on the body of the dynamometer.
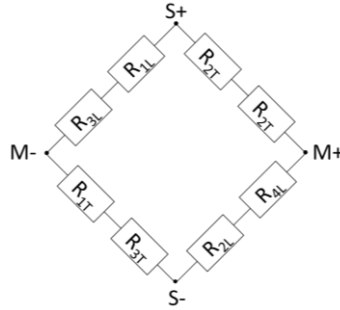
Figure 18 Wheatstone bridge configuration of the strain gauges used for the force measuring setup: S -source, M – measurement

The longitudinal and transversal strain measurements correspond to axial ε_Y and radial strain ε_R, respectively. As such, the millivolt per volt output of the bridge (I) can be expressed using equation (4.12):

$$I = 1000 \times \tag{4.12}$$

$$\left(\frac{R_{1L} + R_{3L}}{R_{1L} + R_{3L} + R_{1T} + R_{3T}} \right.$$

$$\left. - \frac{R_{2T} + R_{4T}}{R_{2L} + R_{2L} + R_{4T} + R_{4T}} \right)$$

On the basis that the resistance (R) of the strain gauge is equal to:

$$R = R_0(1 + k\varepsilon) \tag{4.13}$$

where R_0 is the nominal value of the sensor resistance and k is the gauge factor.

The equivalent analytical solution to the equation (4.12) is given by:

$$I = 1000 \times \frac{k\varepsilon(1 + \upsilon)}{2 + k\varepsilon(1 - \upsilon)} \tag{4.14}$$

where υ is the Poisson's ratio and ε is the analytical axial (longitudinal) strain, which can be calculated as:

$$\varepsilon = \frac{4F}{Ed^2} \qquad (4.15)$$

where F is the applied force, E is the Young's modulus and d is the diameter of the dynamometer.

4.2.1 Dynamometer meshing and data processing

Figure 19 shows the meshing conditions of the dynamometer in ABAQUS. The FEM simulations were run with a 2.5 mm distance between nodes (white circles in Figure 19 left). A 10-node modified quadratic tetrahedron (C3D10M) element was used in this study and implicit analysis was chosen. The 2.5 mm distance between the nodes was selected to provide optimal execution time on a desktop computer. An additional simulation was performed by considering the distance between the nodes as 1 mm. The dynamometer had the properties of a steel alloy: Young's modulus 200 GPa and Poisson's ratio 0.3.

To help with the ease of data collection and postprocessing, the surface of the central part dynamometer on which the strain gauges were mounted was seeded in such way that includes 30 elements (here defined as the space between two seeds) in the axial direction and 36 circumferentially (in Figure 19 the surface edge seeds are represented by the purple triangles). This configuration of surface seeds allows to collect the spatial displacements (U_1, U_2, U_3) at the surface nodes in all three orthogonal directions (X, Y, Z) and their associated positions (in mm), at every 1 mm (nominally) along the axis of the dynamometer and 10 ° radially (or every 1 mm nominally) along the circumference, hence a set of 36 × 31 (1116) surface nodes.

Figure 19 right presents the ABAQUS meshing result of the dynamometer. Worth mentioning that that the size of the strain gauges is larger than the distance between surface nodes (a ratio approximately of 2:1), however, denser sampling can be used to characterise in more detail the dynamometer response.
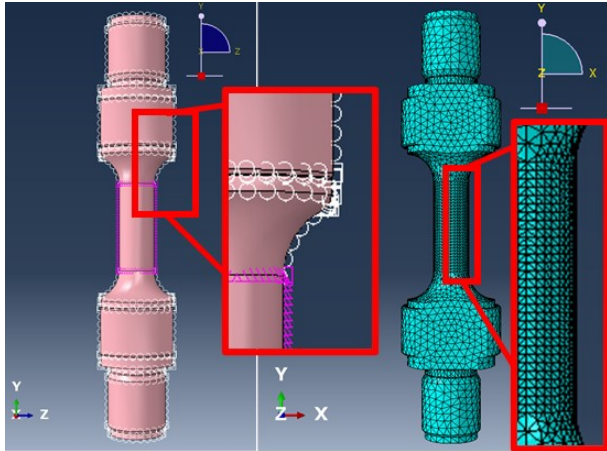
Figure 19: Example of seeding (left) and meshing (right) of the dynamometer

The data was collected along a path that included the surface nodes starting with the top radial data and gradually going down along axial direction of the dynamometer and stored in an excel file (.xls), which was imported in MATLAB (version R2021b Update3) for further processing and analysis. The FEM spatial displacement results stored in the excel files comprised of $6 \times (n+1)$ columns and 1116 rows, n representing the number of loading increments and "+1" to allow storing the data representing the un-loaded state of the dynamometer (0 N).

A diagrammatic indication of the surface nodes of the dynamometer is presented in Figure 20.
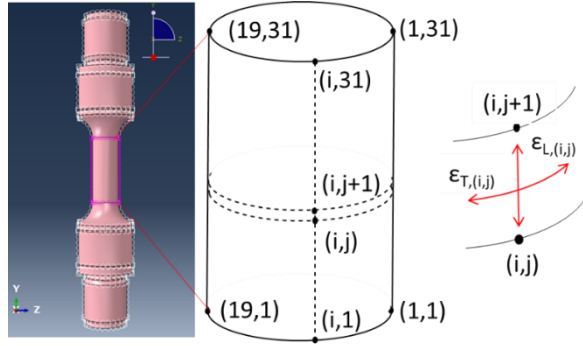
Figure 20: Diagrammatic indication of the surface nodes position on the body of the dynamometer

The longitudinal strain ($\varepsilon_{L,(i,j)}$) – *i.e.* in the axial direction – of a surface between four adjacent surface nodes was calculated using equation (4.16).

$$\varepsilon_{L,(i,j)} = \frac{U_{2,(i,j+1)} - U_{2,(i,j)}}{\Delta Y} \qquad (4.16)$$

where ΔY is nominal axial distance between these two axial nodes, and indices i and j range from 1 to the number of nodes sampled on the circumference (36) and axial number of nodes less 1 (30), respectively.

At each surface node, the radial strain was calculated as the ratio between the square root of the quadratic sum of the node's displacements along the X and Z direction, U_1 and U_3 respectively, and the diameter of the dynamometer, as shown in equation (4.17).

$$\varepsilon_{R,(i,j)} = \frac{2 \times \sqrt{U_{1,(i,j)}^2 + U_{3,(i,j)}^2}}{d} \qquad (4.17)$$

where i and j range from 1 to the number of nodes sampled on the circumference (36) and axially (31), respectively.

The transversal strain ($\varepsilon_{T,(i,j)}$) was calculated using equation (4.18).

$$\varepsilon_{T(i,j)} = \frac{\varepsilon_{R,(i,j+1)} + \varepsilon_{R,(i,j)}}{2} \tag{4.18}$$

Where indices i and j range from 1 to 36 and to 30, respectively.

In the following step, equation (4.12) was used to derive the equivalent mV/V bridge output using the FEM (I_{FEM}) longitudinal and transversal strain results.

$$I_{FEM} = 1000 \times \tag{4.19}$$

$$\left[\frac{2 + k(\varepsilon_{L,(i,j)} + \varepsilon_{L,(i,j+18)})}{4 + k(\varepsilon_{L,(i,j)} + \varepsilon_{L,(i,j+18)} + \varepsilon_{T,(i,j)} + \varepsilon_{T,(i,j+18)})} \right.$$
$$\left. - \frac{2 + k(\varepsilon_{T,(i,j+9)} + \varepsilon_{T,(i,j+25)})}{4 + k(\varepsilon_{L,(i,j+9)} + \varepsilon_{L,(i,j+25)} + \varepsilon_{T,(i,j+9)} + \varepsilon_{T,(i,j+25)})} \right]$$

4.2.2   Strain gauge meshing and data processing

The force strain gauges were implemented in ABAQUS as a sandwich of three thin foils (glue, backing and foil) of 6 mm by 6 mm, positioned on the body of the dynamometer using a type "tie" constraint, with the following properties: Young's modulus of 3.45 GPa, 2.96 GPa and 159 GPa, respectively; Poisson's ratio of 0.3 for glue and backing, and 0.3 for the foil.

The FEM simulations were run with a 0.5 mm distance between nodes (resulting in 650 nodes on each surface of the foil 26 by 25 grid). A 10-node quadratic tetrahedron element (C3D10) was used in this study and implicit analysis was chosen.

The spatial displacements (U_1, U_2, U_3) at the surface nodes of the foils and their associated positions (in mm), were collected in a similar method to the one presented in the previous section.

However, the equivalent sensors output was calculated using the following equation.

$$I_{\text{FEM-SENS}} = 1000 \times$$

$$\left[\frac{2 + k(\varepsilon_{L1,(i,j)} + \varepsilon_{L3,(i,j)})}{4 + k(\varepsilon_{L1,(i,j)} + \varepsilon_{L3,(i,j)} + \varepsilon_{T1,(i,j)} + \varepsilon_{T3,(i,j)})} \right. \tag{4.20}$$
$$\left. - \frac{2 + k(\varepsilon_{T2,(i,j)} + \varepsilon_{T4,(i,j)})}{4 + k(\varepsilon_{L2,(i,j)} + \varepsilon_{L4,(i,j)} + \varepsilon_{T2,(i,j)} + \varepsilon_{T4,(i,j)})} \right]$$

Where the numbers after L and T indices indicate the sensor number.

4.3   Results of FEA of real force transducer

4.3.1   Dynamometer with no sensors

Here, the FEM compression results at 20 kN for 1 mm and 2.5 mm distance between the dynamometer nodes and two loading conditions, concentrated force - Figure 21 a), and pressure - Figure 21 b), is reported.
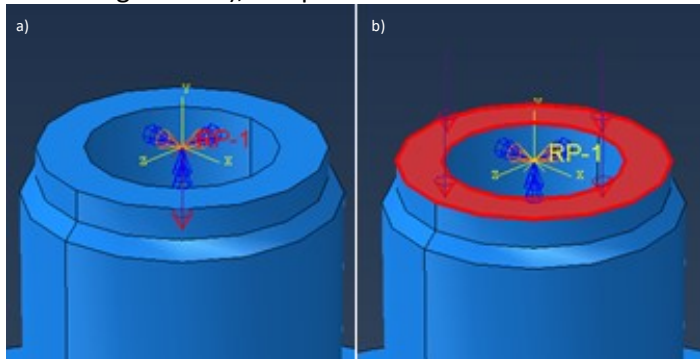

Figure 21: Loading conditions: a) Concentrated force case study; b) Pressure case study

Figure 22 a) shows a cylindrical plot of all the errors in mV/V between the FEM results at 2.5 mm (×) and 1 mm (o) meshing distance for concentrated force case study and analytical solution. The magnitude of these errors decreases from

approximately 32 µV/V for both meshing distances at the far ends of the sampled area on the dynamometer to below 0.05 µV/V and 0.03 µV/V around the middle of the dynamometer for 2.5 mm and 1 mm meshing distance, respectively.

The standard deviation calculated at each axial position decreases from 1.5 µV/V to 1.7 nV/V. As shown in Figure 22 b), the mean errors at each axial position between the FEM results and analytical solution are larger than their associated standard deviations. However, the difference between the average mV/V results for 2.5 mm and 1 mm node distance was larger than their combined standard deviation only in the middle 12 mm of the dynamometer, see Figure 23.

Whilst there are no significant differences between the pressure case study and the concentrated force, the smallest absolute difference between FEM and analytical solution drops to 0.7 nV/V. The pressure case study provides smaller absolute errors in the central 6 mm of the dynamometer as shown in Figure 24.
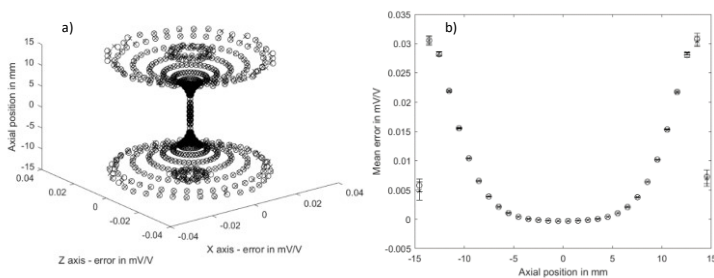

Figure 22 Error maps between FEM compression results at 20 kN, 2.5 mm (×) and 1 mm (o), and the analytical solution in the <u>concentrated force case study</u>: a) all data; b) means and standard deviations (error bars) at each axial position. Axial positions are relative to the middle of the dynamometer
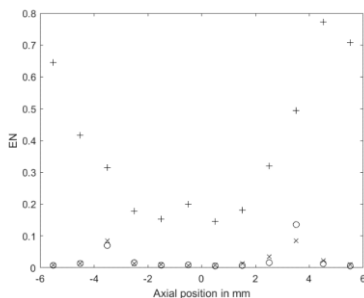
Figure 23 Concentrated force case study at 20 kN – EN is ratio between the standard deviation and the absolute mean error: (×) 2.5 mm nodes distance FEM result relative to the analytical solution, (o) 1 mm and the analytical solution and (+) errors between the two nodes distance FEM results. Axial positions are relative to the middle of the dynamometer

Despite such small differences between the two test cases and analytical solution, there is a significant difference between the two of them, as shown in Figure 25. The difference in mV/V is almost constant in the bottom 20 mm.
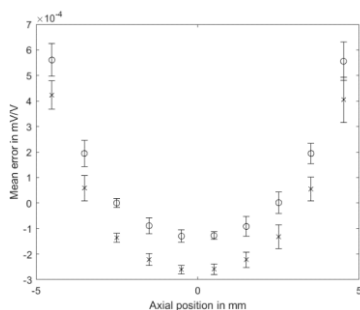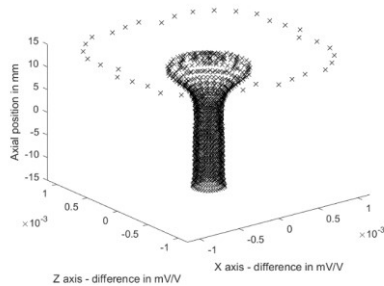

Figure 24 Means and standard deviations (× 10), at the central axial position on the dynamometer, of the errors between the pressure case and the analytical result (o), and the concentrated force and the analytical result (×). All data reported for compression at 20 kN

Figure 25 Difference between FEM results for concentrated force and pressure case study at 20 kN and 2.5 mm node distance

As the FEM mV/V response is derived the longitudinal and radial strain, further plots including the relative mean errors between the FEM and analytical results along the axis of the dynamometer and of the relative errors in the middle of the dynamometer are presented in Figure 26a) and b), respectively.

The FEM dynamometer force response is reported for 2.5 mm distance between the nodes and for a range of compression forces ranging from (0 to 20) kN in 10 % increments, and compared with the real sensor calibration results, which was performed at PTB according to ISO 376:2011-09. Figure 27a) presents the relative mean errors between the FEM results and analytical results, as well as the relative difference between the mean calibration results of the sensor and the analytical solution. Figure 27 b) presents only the non-linearity errors of the FEM and calibration results.
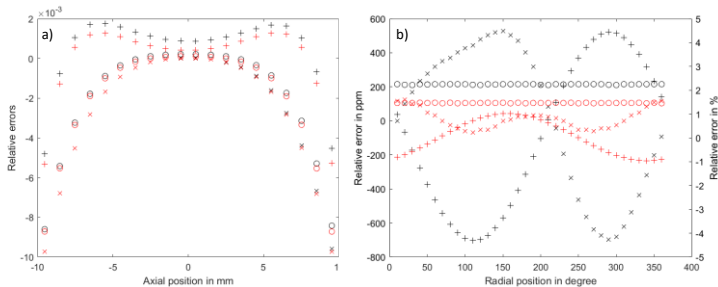
Figure 26 a) Relative mean errors between FEM and analytical results along the axis of the dynamometer; b) Relative errors between FEM and analytical in the middle of the dynamometer (secondary axis in % for radial strain only). Legend: (×) axial strain, (+) radial strain, (o) mV/V indication, black - concentrated force, and red - pressure case study. All data reported for compression at 20 kN and 2.5 mm node distance

Unlike the sensor calibration results, the FEM relative differences from analytical solution do not vary as function of applied force and are just below 0.2 %. Apart from a second order force error (non-linearity), the calibration results are approximately 5.8 % different.

4.3.2   Dynamometer with sensors

Figure 28 presents the difference between the dynamometer FEM results in mV/V with the strain gauges and without (pressure loading conditions, 20 kN and 2.5 mm node distance).

The errors vary from a couple of parts per million at the top end of the dynamometer (15 mm axial position in Figure 28) to about 0.4 % around position on the strain gauges. However, the sensor output was found to be noisy and with large errors around the edges of the sensors.

For comparison, the relative errors of the mV/V output of the dynamometer at 6.5 mm below its centre and the average sensors output calculated from all the results obtained between 0.5 mm above and below that position are shown in Figure 29.
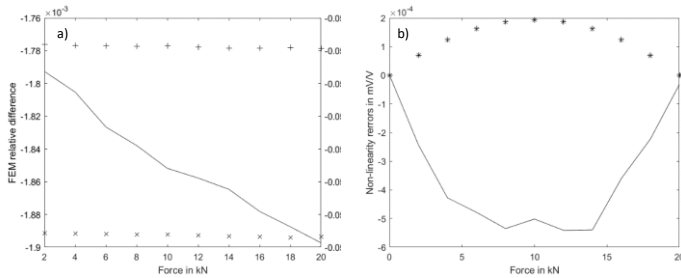
Figure 27 a) Mean relative difference from analytical results 7 mm; b) mean non-linearity errors. Legend: (×) FEM pressure case, (+) FEM concentrated force, continuous line – mean calibration results
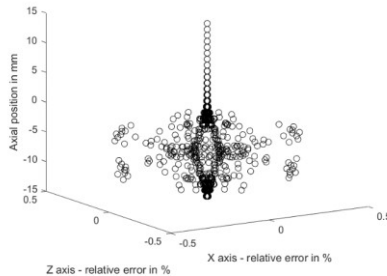
Figure 28 Relative difference between the mV/V output of the dynamometer with and without strain gauges

The difference between sensors output and analytical results was approximately 0.5 % with an associated standard deviation of the mean of 0.12 %.

4.4 Discussions and conclusions

To put the results in the context, the relative uncertainty component associated with the force traceability was 20 ppm, which corresponds to 24 nV/V at 20 kN.
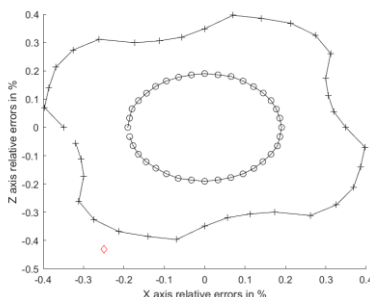
Figure 29 Relative difference between the mV/V output of the dynamometer with (+) and without strain gauges (o), average sensor output (◊) and the analytical solution

From the outset of subsection 4.3.1, the FEM results demonstrated their advantage over the analytical formulation to represent closely the dynamometer response, especially when the shape of the elastic element is not a perfect cylinder. The differences between the FEM and analytical solution, depicted in Figure 22 are always larger than the standard deviation associated with the FEM results, the standard deviation in this case being a measure of the effect of the spatial reproducibility FEM results. However, FEM requires very careful implementation which is especially important in the DT of measurement uncertainty context, from meshing to sampling and from choosing the correct constitutive models to extract/ visualise the results. For example, in this study only two node distances were studied, 2.5 mm and 1 mm, simulations form smaller meshing distances being nearly impossible to run in an average computer. The difference between the results obtained for these two meshing conditions being comparable with the top end traceability contribution (see Figure 23 and Figure 24). Much larger differences in results were recorded for different loading conditions, with magnitudes in the order of tens of a percentage at the lower end of the dynamometer to one

percent of the reproduced values at the top end, as shown in Figure 25, highlighting potential effects of the loading set up.

However, the mV/V equivalent results present less errors compared to the individual strain values from which they are derived, as shown in Figure 26, highlighting the potential numerical errors arising from the approximations performed in FEM, and in this case their effect on the radial position of the surface nodes. The way in which the sensors are connected in practice to measure the force without the bending effect seems to remove the effect of the FEM numerical errors.

Nevertheless, the sensor calibration results did not match the expected non-linear behaviour of the mV/V output (see Figure 27). This discrepancy is likely to originate from the strain gauges output, which has been addressed in subsection 4.3.2. The FEM results are affected by the presence of the strain gauges as shown in Figure 28 and Figure 29, which may change significantly with the type of constraint, subject of future work. However, the FEM non-linear errors do not change in the presence of the gauges attached to the dynamometer, meaning that the present configuration of the FEM is not able to predict current behaviour of the sensor.

Here we have investigated the FEM potential to become an integral part of a metrological DT [25] of a force device and, besides the discrepancies between the experimental and analytical results which require further investigations, we have shown that the Nevertheless, the next steps are focused on the conceptualisation of the DT [34], *i.e.* integrating the FEM model into a metrology decision making process.

5 Continuous calibration test model

In the following section the FEA model of continuous calibration test of a 20 kN load cell is presented. The description of the continuous calibration test procedure is followed by the ANSYS model implementation. The FEA is then compared with the measured data of the force transducer during creep test.

5.1 Continuous calibration test procedure

In continuous calibration, a force measurement device is calibrated in a machine that can control the force loading and unloading operation as a function of time. A specific example is the creep test performed at the end of the static procedure in which the transducer is loaded at full scale and held for five minutes. Values are taken at thirty seconds and five minutes after loading the transducer. The creep is measured without the load, but only after 5 min after the load is removed [8]. Corresponding loading profile of a creep test with the nominal force of 20 kN is presented in Figure 30.
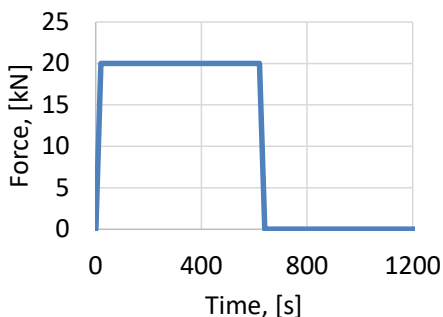
Figure 30 Force vs time profile for continuous tests

The measured output signal of the force transducer tested following the creep procedure is presented in Figure 31. The test

was performed on tension with the filter settings of 1.7 Hz Bessel and samplerate of 5-10 Hz.
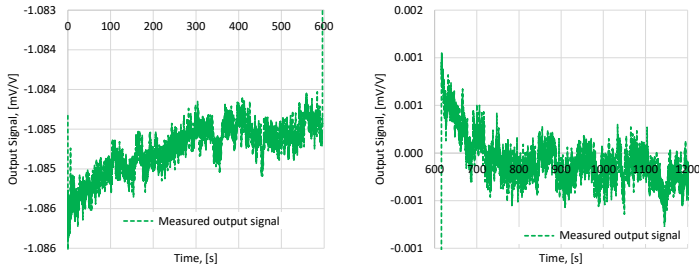
*Figure 31 Measured output signal of the force transducer after creep test at 20 kN nominal force: a) during holding stage after full loading; b) during holding stage after full unloading*

The strain gauge output signal increased after the maximum load was applied, until reaching a steady value. After removing the load, the output signal of the strain gauge drops as well, but due to creep one can see the residual output signal value, which then creeps to the zero value after some time. The stain gauge phenomenon is described in details in [35].

5.2   Continuous calibration test model

The geometrical model of the transducer presented in Figure 32 is used to build a FE-model of a dynamic calibration test. The improved load cell setup without masses is used [33]. An element size of 6e-4 m was used to mesh the entire model. The measurement region of the load cell was meshed with the structured hexahedral elements. Free triangular mesh was used on the rest of the load cell to decrease computational costs.
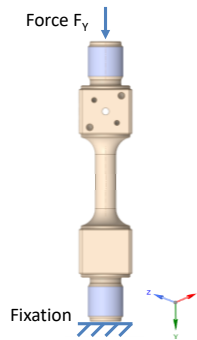
Figure 32 Geometrical model of the force transducer and strain gauges with the applied boundary conditions and load

The coupled field transient analysis of ANSYS software was used model structural as well as thermal strains during continuous calibration process. Thermal as well as structural physical properties were prescribed to the load cell.

Time step size showed to have a great effect on the solution convergence and calculated temperature. Time integration was set in the following manner ensured stable convergence of the analysis:

- initial time step was set to be 100 times smaller than the length of the loading step;
- minimum time step was set to be 1000 smaller than the loading step;
- maximum time step was set to be 10 times smaller than the loading step.

In addition to the elastic material properties required for static structural analysis, the thermal properties for load cell material were defined according to [36].

The creep force load was applied in *Y* axial direction. Force profiles, representing the last creep loading step, see Figure 30, were used to decrease computational time. The ambient

temperature was set to 22 °C. Convection condition was defined with the heat transfer coefficient set to 25 [W/m²·°C] equal to all surfaces of the load cell.

5.3   Simulation results of creep test

In order to compare the simulations with the experimental results, the thermal and elastic strains were calculated in the middle region of the load cell, where the strain gauges are placed. The simulated thermal strains, Figure 33, as well as elastic strains, Figure 34, are presented below.
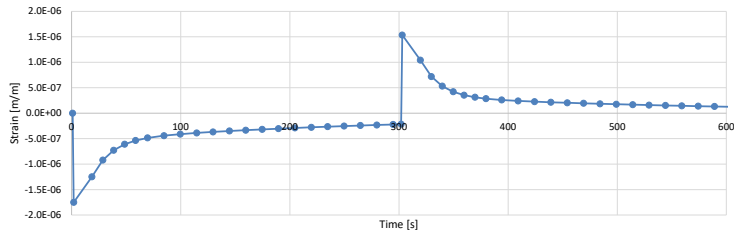
Figure 33 Simulated thermal strains in the strain gauge placement region of the load cell during creep cycle
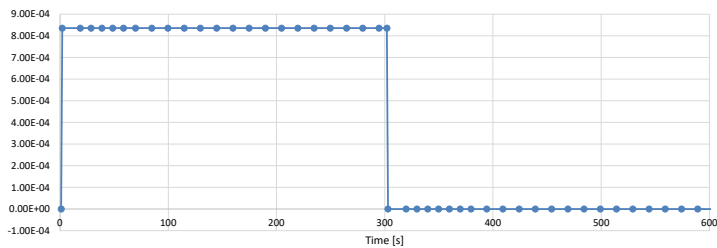
Figure 34 Simulated elastic strains in the strain gauge placement region of the load cell during creep cycle

Total strains are calculated as the sum of elastic and thermal strains. Similar to static calibration test model, the FEA output signal lies close to the analytical value, which is twice higher that the experimental one. To enable better data comparison the

measured as well simulated output signals were normalised using the formula (5.1):

$$X' = \frac{X - X_{min}}{X_{max} - X_{min}} \tag{4.17}$$

The simulated output signal of the load cell is presented in Figure 35. The output signal was calculated using the approach discussed in section 4 in details.
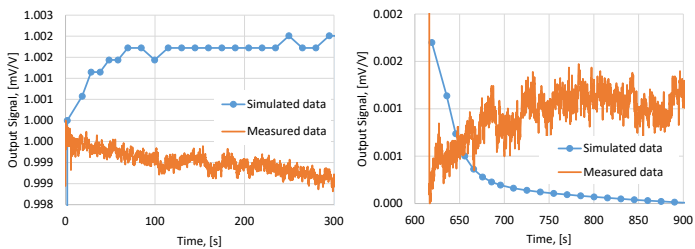
Figure 35 Comparison between the simulated and the measured data during loading (left hand side) and unloading (right hand side) stages

The simulated and measured data show opposite trends. The measured data represents the strain gauge output signal and the simulated one the output of the load cell. This is in accordance with the findings of Kühnel, who stated that the creep recovery of the load cell acts in opposite direction to the creep of the strain gauge and the corresponding glue layer [37].

6 Dynamic calibration test model

To study the influence of the frequency on the output signal during dynamic calibration test a dynamic FE-model presented in section 5 was further developed to address the dynamic calibration conditions.

6.1 FE-model set up

The FE-model of a dynamic calibration test was built as described is subsection 5.2. Axial load was applied in a cyclic way with two loading rates of 0.1 and 1 seconds as it is shown in Figure 36. Three loading cycles were simulated in order to maintain a reasonable simulation time.
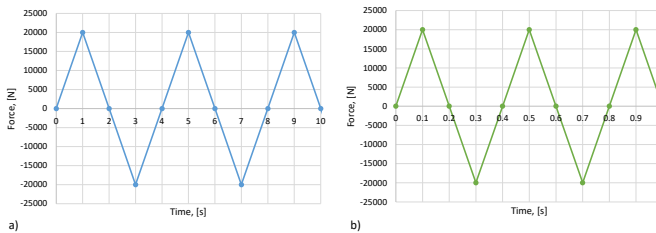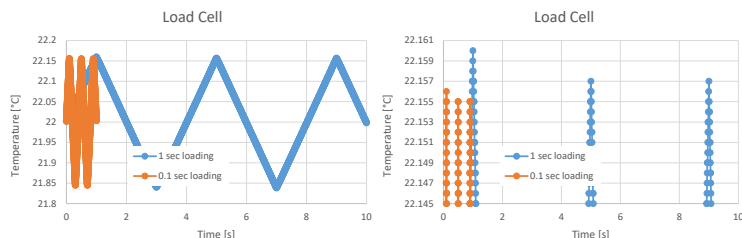

Figure 36 Simulated dynamic calibration profile with the loading rate of a) 1 second and b) 0.1 second

6.2 Simulation results

The FEA temperature profiles corresponding to two loading cycles with different loading rates are presented in Figure 37.

Figure 37 Simulated temperature profile during dynamic calibration process: a) full range view; b) high temperature resolution view, showing detailed temperature change at maximum temperatures

The profiles for both loading rates show a slight decrease of the temperature peaks for the second and third cycles. The fluctuation of the temperature due to thermoelastic effect during cyclic loading is of about 0.15 °C. The simulation temperature fluctuation shows good agreement with the cyclic test on AISI 1045 mild steel cylindrical specimens, reported in [38], where temperature fluctuation of a specimen of 0.12 °C was observed.

Due to extremely high computational costs of the dynamic calibration test model, FEA is not suitable to fully analyse the dependency of the dynamic sensitivity of the force transducer on mass and frequency, described in [8]. Thus, for a proper application in DMT, an investigation into the use of Machine Learning could be beneficial.

7 Conclusions

The work described in this report has covered the development of digital constructs necessary for the digital metrological twin of a force transfer standard in relation to its static, continuous and dynamic on based on FEA and analytical modelling.

The DT concept for a force transfer standard has been advanced in sections 2 and 3 of this report and covered two complementary DT perspectives: one that looks at assuring safe metrological use of the force device experiencing over loading and one that describes the metrological assurance in relation to the results reporting.

The FEA model for static measurement of a force transfer standard was presented in section 4, together with an analytical formulation, which allowed to validate the use of the static model in the evaluation of the effect of non-compliant loading and unloading such as bending moments, tilt and side forces to the measurement uncertainty. The experimental validation was deemed not sufficiently accurate to validate the proposed model, especially due to the relaxation of the supporting matrix, previously reported in the literature as the main source of creep.

Section 5 addresses the thermal of creep previously recorded in literature as the thermo-mechanical effect. The findings are in agreement with the current knowledge about the creep behaviour experienced in force transducers. The creep evaluated in [8] was governed by the strain gauge relaxation behaviour mentioned above. Nevertheless, the model is able to estimate the temperature fluctuation and its effect on the strain measurements, which can be used to decouple the strain gauges relaxation effect from the thermomechanical beam behaviour.

Section 6 presents the FEM model that is used to evaluate the sensor behaviour under cyclic loading, but it was discovered that effectiveness of the simulations was hindered by the computational limitations required by FEA. A responsive solution will rely on a surrogate model that is validated by an FEA and a different experimental setup.

A difficulty that was not overcome in this work was accurate modelling of the strain gauge behaviour. The main efforts were concentrated at developing a comprehensive computational model of the entire device. The drawback of the model was rooted in the relative mismatch between the element size required to simulate the beam response and the strain sensor response. Future work could look into different modelling strategies which can assess the strain gauge real behaviour. Nevertheless, the methods of determining experimentally the creep behaviour of the strain gouges can be used to determine a comprehensive force sensor measurement model. Given the variability in the sensors output, AI technologies could be used along the current and past experimental studies to predict the strain gauges creep behaviour in the future.

Here a GUM S1 Monte Carlo approach can use the models developed in this work, which estimate the influence of the sensor position on the body of the dynamometer, bending moments, tilt and side forces to the transfer standard measurement output, to establish summary uncertainty information, means and standard deviations, associated with these influence parameters and propagate them with an updated measurement model. In this way, the transfer standard calibration will be less reliant on a black-box approach and will be able to use AI techniques in the future, which will enable the prediction of the strain gauges output, ultimately improving the force standards' accuracy.

8 References

[1]   W. D. Callister and D. G. Rethwisch, Material Science and Engineering, Ninth. John Wiley & Sons (Asia) Pte Ltd, 2015.

[2]   A. Hunt et al., "Guide to the Measurement of Force," London, 1998.

[3]   A. Rao, J. Voyles, P. Ramchandani and R. Adam, Top 10 artificial intelligence (AI) technology trends. 2017

[4]   A. Detzner, and M. Eigner, A digital twin for root cause analysis and product quality monitoring. 1547-1558. 10.21278/idc.2018.0418. 2018

[5]   NASA, "NASA Technology Roadmaps TA11 - Modeling, Simulation, Information Technology and Processing" 2015.

[6]   Kraft, Edward. The Air Force Digital Thread/Digital Twin - Life Cycle Integration and Use of Computational and Experimental Knowledge. 2016

[7]   E. Glaessgen and D. Stargel, The Digital Twin Paradigm for Future NASA and U.S. Air Force Vehicles. https://doi.org/10.2514/6.2012-1818. 2012

[8]   J. Sander, D. Mirian, H. Frank, S. Hassan, R. Kumme, A. Prato et al. Validation report which details the advanced models developed to describe a) static and continuous and b) dynamic force transfer standards taking into account sensitivity stability, temperature and other parasitic influences on the measurement uncertainty (target uncertainty is 1 % up to 100 Hz and 2 % between 100   -   1000   Hz)   Zenodo. https://doi.org/10.5281/zenodo.7113187, 2022

[9]   Total Materia, "Creep and Stress Rupture Properties," 2010. https://www.totalmateria.com/page.aspx?ID=CheckArti

cle&site=kts&NM=296 (accessed Jul. 22, 2019).

[10] H. Sato, K. Omote, and A. Sato, "Extrapolation of Creep Curve and Creep Rate by Strain Acceleration Parameter in Al-Mg Solid Solution Alloys," Mater. Sci. Forum, vol. 794–796, no. 2, pp. 307–312, 2014, doi: 10.4028/www.scientific.net/msf.794-796.307.

[11] K. Bowman, Mechanical Behavior of Materials, Wiley Inte. Danvers, MA: John Wiley & Sons, 2004.

[12] J. Li and A. Dasgupta, "Failure-Mechanism Models for Creep and Creep Rupture," IEEE Trans. Reliab., vol. 42, no. 3, pp. 339–353, 1993.

[13] R. Kolhapure, V. Shinde, and V. Kamble, "Geometrical optimization of strain gauge force transducer using GRA method," Meas. J. Int. Meas. Confed., vol. 101, pp. 111–117, 2017, doi: 10.1016/j.measurement.2017.01.030.

[14] OIML, Metrological regulation for load cells - Part 1: Metrological and technical requirements, 2021st ed. Paris: OIML, 2021.

[15] A. H. Bracket et al., Strain Gage Users' Handbook. Elsevier Science Publishers, Ltd., 1992.

[16] T. P. Kieffer, "Analysis of Creep Behaviour of Bending Beam Load Cell," Adv. Exp. Mech., vol. 3, pp. 157–160, 2018.

[17] M. Reith et al., "FZKA 7065 Creep of the austenitic steel AISI 316 L (N) – Experiments and Models," Postfach, Karlsruhe, 2004.

[18] A. K. Asraff, R. Aparna, D. Kumaresan, and R. Muthukumar, "Comparison of creep properties of four copper alloys and creep based stress analysis of a rocket engine combustion chamber," in Procedia Engineering - 6th International Conference on Creep, Fatigue and Creep-Fatigue Interaction, 2013, vol. 55, pp. 45–50, doi: 10.1016/j.proeng.2013.03.217.

[19] X. Wu and M. Pecht, "Material Testing for Polyimides," CALCE EPRC, University of Maryland, 1993.

[20] Dupont, "DuPont TM Kapton ®," Midland, Michigan, 2017. [Online]. Available: http://www.dupont.com/content/dam/dupont/products-and-services/membranes-and-films/polyimde-films/documents/DEC-Kapton-summary-of-properties.pdf%0Ahttp://www.dupont.com/content/dam/dupont/products-and-services/membranes-and-films/polyimde-films/documents/.

[21] T. Kopczynski and D. Ness, "White Paper: Five Factors that can Affect Your Weighing System's Accuracy," San Diego, California, 2011.

[22] SmartCom - Communication and validation of smart data in IoT-networks. [Online]. Available: https://www.ptb.de/empir2018/ smartcom/project/ (accessed: Feb. 15 2021).

[23] D. Hutzschenreuter, F. Härtig, W. Heeren, T. Wiedenhöfer, Forbes A., and C. Brown et al., "SmartCom Digital System of Units (D-SI) Guide for the use of the metadata-format used in metrology for the easy-to-use, safe, harmonised and unambiguous digital transfer of metrological data," in Zenodo. Accessed: Feb. 15 2021.

[24] T. Mustapää, J. Taponen, O. M. Maennel, D. Hutzschenreuter, W. Heeren, and C. Brown et al., Guideline describing the concept of UniTerm and how to establish secure communication interfaces in legal metrology (2.0). [Online]. Available: https://doi.org/10.5281/zenodo.5704676 (accessed: October 2022).

[25] F. Härtig, "VirtMet applications and overview," Berlin, Sep. 21 2021.

[26] W. Heeren, B. Müller, G. Miele, T. Mustapää, D.

Hutzschenreuter, and C. Brown et al., "SmartCom – Key Findings for Digitalisation in Metrology," 2021 IEEE International Workshop on Metrology for Industry 4.0 IoT (MetroInd4.0 IoT), pp. 364–369, 2021, doi: 10.1109/MetroInd4.0IoT51437.2021.9488450.

[27] M. W. Grieves, "Virtually Intelligent Product Systems: Digital and Physical Twins," in Complex Systems Engineering: Theory and Practice.

[28] B. Piascik, J. Vickers, D. Lowry, S. Scotti, J. Stewart, and A. Calomino, "DRAFT Materials, Structures, Mechanical Systems, and Manufacturing Roadmap: Technology Area 12," National Aeronautics and Space Administration, Nov. 2010.

[29] Digital Calibration Certificate - https://www.ptb.de/dcc/ (accessed 17 November 2022)

[30] ANSYS, Inc., "Scripting in Mechanical Guide," U.S.A., ansyshelp.ansys.com, (accessed 15 Jul. 2022

[31] M. Smith, ABAQUS/Standard User's Manual, Version 6.9: Dassault Syst. Sim. Corp., USA, 2019.

[32] ISO 376 Metallic materials — Calibration of force-proving instruments used for the verification of uniaxial testing machines: ISO, Switzerland, 2011

[33] A. Nitschke, et al., „Entwicklung eines Kraft-Transfernormals für die Kalibrierung periodischer Kräfte in Werkstoffprüfmaschinen mit Quantifizierung parasitärer Einflussgrößen", ITG-Fachbericht 303 – Sensoren und Messsysteme, Beiträge der 21. ITG/GMA-Fachtagung, 10.-11. Mai 2022 in Nürnberg, VDE Verlag, 2022, ISBN 978-3-8007-5835-7, S.63-73.

[34] L. Wright, S. Davidson, "How to tell the difference between a model and a digital twin" Adv. Model. and Simul. in Eng. Sci, vol. 7, no. 13, pp. 1–13, 2020.

[35] S. Keil, Dehnungsmessstreifen. Springer Vieweg

Wiesbaden. https://doi.org/10.1007/978-3-658-13612-3. 2017

[36] Ovako, STEEL NAVIGATOR – find the right steel for your needs: 30CrNiMo8. https://steelnavigator.ovako.com/steel-grades/30crnimo8/, (accessed 15 July 2022).

[37] M. Kühnel, "Traceable measurement of the mechanical properties of spring bodies for force measurement technology," [in German], PhD thesis, Technical University Ilmenau, 2013.

[38] Lee, H.T., Chen, J.C. & Wang, J.M. Thermomechanical behaviour of metals in cyclic loading. JOURNAL OF MATERIALS SCIENCE 28, 5500–5507 (1993). https://doi.org/10.1007/BF00367821

The content presented was developed within the framework of the EU-funded project ComTraForce " Comprehensive traceability for force metrology services " *with the* support of international partners from science and industry.

https://www.ptb.de/empir2019/comtraforce/home/